ADVANCED FUNCTIONAL MATERIALS
www.afm-journal.de

www.MaterialsViews.com

The Size Dependence of Hydrogen Mobility and Sorption Kinetics for Carbon-Supported MgH_2 Particles

*Yuen S. Au, Margo Klein Obbink, Subramanian Srinivasan, Pieter C. M. M. Magusin, Krijn P. de Jong, and Petra E. de Jongh**

MgH_2 is a promising material for reversible solid-state hydrogen storage. It is known that particle size can have a strong impact on hydrogen dynamics and sorption characteristics, but more detailed insight has been hampered by the great challenge to prepare small and well-defined particles and study their hydrogen storage properties upon cycling. The preparation of MgH_2 nanoparticles supported on high surface area carbon aerogels with pore sizes varying from 6–20 nm is reported. Two distinctly different MgH_2 particle populations are observed: X-ray diffraction invisible nanoparticles with sizes below 20 nm, and larger, crystalline, MgH_2 particles. They release hydrogen at temperatures 140 °C lower than bulk MgH_2. The size-dependent hydrogen kinetics is for the first time corroborated by intrinsic hydrogen dynamics data obtained by solid state ^{1}H NMR. Fast cycling is possible (80% of the capacity absorbed within 15 min at 18 bar and 300 °C), without a change in the hydrogen sorption properties, showing that the growth of the nanoparticles is effectively prevented by the carbon support. A clear correlation is found between the hydrogen desorption temperature and the size of the MgH_2 nanoparticles. This illustrates the potential of the use of supported nanoparticles for fast, reversible, and stable hydrogen cycling.

1. Introduction

Nowadays, more than 60% of the energy is obtained from fossil fuels.[1] The current status of the world-wide energy reserves and increasing energy consumption makes it necessary to move towards alternative sources for energy production. Renewable energy sources, like solar and wind energy, are required to deal with the current environmental issues, such as global warming. The renewable energy sources usually provide electricity while we also need fuels as energy carrier for off-grid applications. Hydrogen is proposed as alternative energy carrier.[2] However, an important challenge is the reversible storage of hydrogen, which has to be done safely and with high density. Hydrogen storage in metals or other solid compounds has the potential to satisfy these conditions.

MgH_2 has been widely studied as a potential hydrogen storage material. The low cost of the material and its high hydrogen storage capacity of 7.6 wt% are interesting for stationary and mobile energy storage applications. MgH_2 can store hydrogen reversibly following the reaction:

$$Mg(s) + H_2(g) \rightleftarrows MgH_2(s) \tag{1}$$

The related decomposition enthalpy is 75 kJ mol^{-1} H_2,[3,4] which means that hydrogen release only occurs above 300 °C at 1 bar H_2, which is the thermodynamic equilibrium temperature for the reaction at that pressure. The high operation temperature is a drawback; however, this will not be a problem if the material can be combined with exothermic processes.[5] Prototypes of storage tanks with efficient heat management have already been realized.[6] Nonetheless, thermodynamic and kinetic enhancement of the Mg-system is still desirable for mobile applications.

Modification of the reaction equilibrium is often obtained by adding other compounds. The compounds either form a stable Mg-alloy upon dehydrogenation or involve a ternary hydride. Examples of these systems include Mg–Al [7] or Mg_2NiH_4,[8] but the enthalpy required to decompose the hydrides is still high in the range of 60 kJ mol^{-1} H_2. Computational studies have predicted that MgH_2-clusters consisting of few atoms would have lower thermodynamic stability [9–11]. However, experimental results only show modest changes in the thermodynamic equilibrium, since the less positive value for the enthalpy for desorption is being counteracted by a less positive value for the entropy change.[12]

Another issue is the slow reaction kinetics. The kinetic properties can be changed by modifying the size of the Mg particles.

Y. S. Au, M. K. Obbink, Prof. K. P. de Jong,
Dr. P. E. de Jongh
Inorganic Chemistry and Catalysis,
Debye Institute for Nanomaterials Science
Utrecht University
Universiteitsweg 99
3584 CG Utrecht, The Netherlands
E-mail: p.e.dejongh@uu.nl

Dr. S. Srinivasan
Department of Chemical Engineering and Chemistry
Eindhoven University of Technology Postbus 513
5600 MB, Eindhoven, The Netherlands

Dr. P. C. M. M. Magusin
Centre for Surface Science and Catalysis
KU Leuven
Kasteelpark Arenberg 23 – bus 2461
3001, Leuven, Belgium

DOI: 10.1002/adfm.201304060

Decreasing the particle size to nanoscale enhances the reaction kinetics due to a larger surface-to-volume ratio of the particle and decreased solid-state diffusion distances for hydrogen.[13] However, so far it is not clear what the rate-limiting step is for hydrogen release and which effect dominates the kinetic enhancement or whether both effects are contributing.

Different approaches have been investigated to synthesize nanostructured MgH_2. Ball milling with addition of catalysts is often used to create nanostructured materials. For example, addition of metals such as Pd and Ni or metal oxides like Nb_2O_5 has proven to be quite effective.[14–20] Despite the kinetic enhancement, high temperatures are still required for the hydrogen sorption reactions to occur. Particle growth occurs at these elevated temperatures and deteriorates the kinetic properties.[21] To prevent particle growth, direct inter-particle contact has to be avoided. One strategy to achieve this is to anchor nanoparticles on porous and/or high surface area support materials. The porous structure of the support material allows potentially control over the particle size.[22–25]

In this study we show the importance of size effects on the hydrogen sorption kinetics in Mg and MgH_2. To gain more insight in the kinetic behavior of pure $Mg(H_2)$ nanoparticles, we used carbon supports with different pore size distributions and obtained a significant fraction of MgH_2 nanoparticles limited to a specific size range between 6–20 nm. The use of carbons with different pore sizes allowed for the first time systematic control over the nanoparticle size of MgH_2. We also found that the supported MgH_2 nanoparticles exhibit remarkably different hydrogen sorption properties compared to bulk MgH_2 and this coincides with different intrinsic H-mobilities as determined with ^1H solid-state NMR.

2. Results and Discussion

2.1. MgH_2-Carbon Aerogel Nanocomposites

The average pore diameters of the carbon supports were calculated by averaging the volume contribution of the available mesopores (2–50 nm) from the mesopore size distribution as determined by N_2-physisorption (Figure S1, Supporting Information). This resulted in average pore sizes of 6 nm, 9 nm, 12 nm, and 20 nm (**Table 1**).

Table 1. The average pore diameters of the carbon scaffold and the average small nanoparticle SNP size of MgH_2 are shown. The mesopore volumes of the carbon aerogels before and after addition of Mg; and after removal of Mg are also reported.

Sample	Avg. Pore Size [nm]	V_{meso} [$cm^3\ g^{-1}$]	$V_{meso}MgH_2$ [$cm^3\ g^{-1}$]	Avg. MgH_2 SNPs size [nm]
CA-6	6	0.16	0.11	6.3(±1.8)
CA-9	9	0.46	0.33	7.2(±2.1)
CA-9 leached	9	0.45	–	–
CA-12	12	0.72	0.65	9.2(±2.0)
CA-20	20	1.14	0.97	12.9(±3.0)

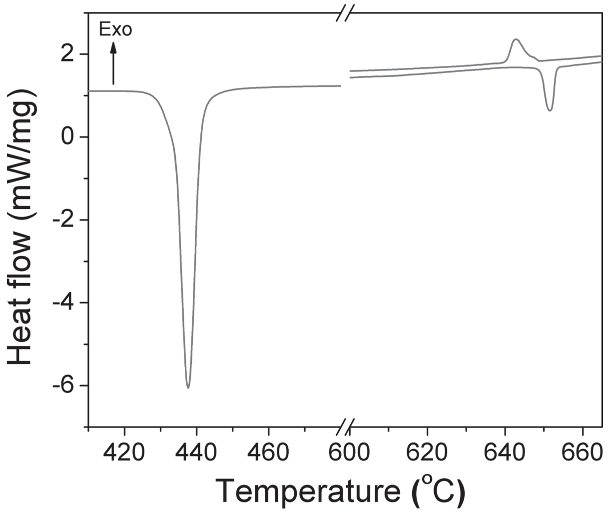

Figure 1. DSC measurement starting with a 10 wt% MgH_2 and CA-9 physical mixture heated under Ar with 5 °C min^{-1}. Around 435 °C the endothermic decomposition of MgH_2 to Mg is observed and around 650 °C the melting of Mg and subsequent exothermic solidification during cooling occurred.

Figure 1 shows the result of the in-situ study on the heat treatment of a physical mixture of MgH_2 with CA performed with DSC. Upon heating, an endothermic event with an onset temperature near 430 °C was observed. This was due to the decomposition of MgH_2 to metallic Mg. Another endothermic event occurred around 650 °C, which is the melting point of Mg. During cooling, an exothermic signal was observed with the same onset temperature as the melting point corresponding to solidification of Mg. This peak was broader compared to the peak observed during melting probably due to nucleation required for recrystallization. No other peaks were found indicating that no reaction took place between Mg and the carbon support during the heat treatment.

The carbon supports were non-crystalline and X-ray diffraction only showed one broad diffraction peak around 50° (**Figure 2**a). Figure 2b shows a physical mixture of the CA support with 10 wt% pure MgH_2. The X-ray pattern of the Mg-CA sample after heat treatment (Figure 2c) only had peaks belonging to the hexagonal Mg phase ($P6_3/mmc$) and the broad peak corresponding to the amorphous carbon aerogel. The presence of sharp Mg diffraction lines indicated that crystalline Mg is present. After hydrogenation, X-ray diffraction was measured again and Figure 2d shows that new diffraction lines appeared belonging to the tetragonal MgH_2 phase ($P4_2/mnm$). Thus, the crystalline fraction of Mg was rehydrogenated to form MgH_2. However, the overall intensity of the diffraction lines of the nanocomposite was much lower than for a physical mixture of MgH_2 and CA (Figure 2b) with the same weight ratio. A significant fraction of MgH_2 was not detected, which is in line with earlier findings.[26] According to analysis with Rietveld refinement, 70% of the Mg added was detected as crystalline Mg (Figure S2, Supporting Information). This suggests that 30% of the Mg is nanocrystalline or amorphous and cannot be probed by XRD due to lack of long range order. Another possibility is that some Mg was evaporated during heating due to its high vapor pressure.

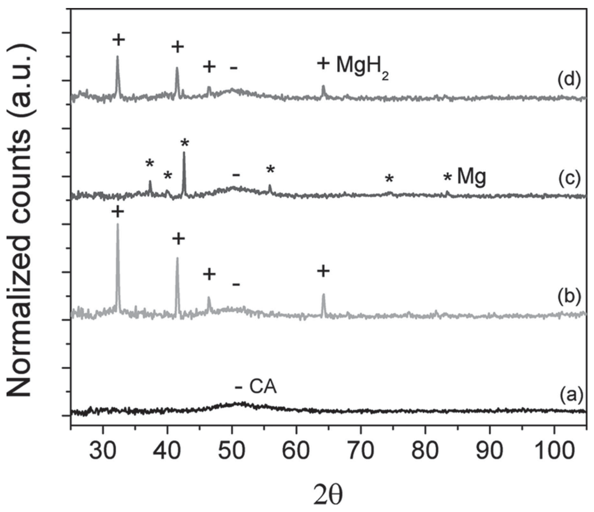

Figure 2. XRD patterns of a) CA-9 as synthesized, b) a physical mixture of CA-9 and 10 wt% MgH_2, c) 10 wt% Mg/CA-9, and d) 10 wt% MgH_2/CA-9. The used symbols indicating the diffraction lines are: CA (–), Mg (*), and MgH_2 (+). The intensities are normalized to fit in the same scale for comparison.

Figure 3 shows a bright field TEM image of the MgH_2/CA-6 composite and interestingly, many nanoparticles are observed. EDX measurements confirm that these particles are MgH_2 species (Figure 3b). Additionally, the presence of large MgH_2 crystallites was confirmed by TEM (Figure S6, Supporting Information). It is clear that MgH_2 particles were formed in two distinctly different size ranges: small nanoparticles (SNPs) with a size smaller than 20 nm, but also larger nanoparticles (LNPs) in the range of 100 nm that can be detected as crystalline MgH_2 with XRD. The average nanoparticle sizes of MgH_2/CA-6, MgH_2/CA-9, MgH_2/CA-12, and Mg/CA-20 were 6.3 nm (±1.8), 7.2 nm (±2.1), 9.2 nm (±2.0) and 12.9 nm (±3.0) respectively (Figure 3d–f). Using scaffolds with larger pore sizes resulted in larger particles, while in all cases the resulting particle sizes were somewhat smaller than the average scaffold pore diameter.

Table 1 summarizes the structural properties of the CA supports and the SNPs of MgH_2. Upon heat treatment with Mg, the pore volume of the CAs decreased (Figure S4, Supporting Information).The initial pore volume was recovered after removal of Mg (Figure S5, Supporting Information). Hence, deposition of Mg did not change the structure of the carbon. The decrease in pore volume is caused by Mg nanoparticles being inside the pores of CA.

2.2. The Influence of Particle Size on the Hydrogen Release Kinetics and H-Mobility

The hydrogen release profile of MgH_2/CA-9 was compared to that of MgH_2 powder and MgH_2 on High Surface Area Graphite (HSAG) in **Figure 4**. Pure MgH_2 (a) released hydrogen above 400 °C. If MgH_2 powder was physically mixed with CA, no significant change in the hydrogen release profile was observed (b). When MgH_2 was supported on HSAG-500 (c), the peak temperature was lowered to 386 °C. The hydrogen desorption profile of the MgH_2/CA-9 sample was quite different (Figure 4d). Two peaks were observed. One peak had a maximum temperature in a similar region as HSAG-500, which was around 380 °C, and can probably be attributed to the hydrogen release from the LNPs of MgH_2. More interesting is the presence of a peak around 280 °C, which was ≈140 °C lower than for bulk MgH_2. This desorption temperature is comparable to MgH_2 supported on CA or CMK-3, prepared by solution impregnation,[27–30] and hence can probably be attributed to the SNPs of MgH_2 present in the pores of the carbon scaffold.

This was further supported by the fact that there was a modest, but significant, shift of the low temperature release for the different MgH_2/CA composites (**Figure 5**, left). The lowest peak temperature was observed for CA-6, which is the carbon support with the smallest average pore size, followed by CA-9, CA-12, and CA-20 with the peak maximum at the highest temperature. This trend is visualized in Figure 5 (right), which shows the maximum peak temperatures against the average size of the MgH_2 nanoparticles (Figure 3).

In all samples, MgH_2 was the only phase that could release hydrogen, as no impurities were detected. A significant shift in equilibrium decomposition temperature is unlikely in this size range, so the correlation between size and temperature shift is most likely a kinetic effect, but the exact underlying cause of this correlation is not fully understood. It is generally postulated that either the surface association/dissociation of hydrogen, and/or slow solid state hydrogen diffusion are rate-limiting steps.[25] Therefore we decided to study the hydrogen dynamics for the different particle sizes. These can be measured by solid-state ^{1,2}H NMR; a powerful tool to investigate nanostructured phases as it does not depend on long range order, but probes local properties.[32]

Figure 6a–d shows static ^{1}H NMR spectra of the composites MgH_2/CA-6, MgH_2/CA-9, MgH_2/CA-12, and MgH_2/CA-20 (thick black lines). The NMR line shapes were broad (FWHH ≈ 20 kHz) as result of the strong dipole coupling between ^{1}H nuclei in the MgH_2 nanodomains. However, these were not as broad as the static NMR line shape of bulk MgH_2 (FWHH ≈ 40 kHz), which has been superimposed (grey lines) on the spectra of the four composites in Figure 6a–d, for comparison. The significantly narrower ^{1}H NMR resonances of the nanocomposites reflected the motional-averaging effect caused by hydrogen mobility inside the MgH_2 nanodomains. The more mobile the hydrogen atoms, the more their (average) dipole interactions are reduced and the narrower the ^{1}H NMR resonance become.

The increased hydrogen mobility in the nanocomposites was confirmed by ^{1}H NMR spin-lattice relaxation, which is sensitive to mobility at the 10^{-12}–10^{-8} s^{-1} timescale. The higher the mobility, the faster this type of relaxation becomes. Indeed, the spin-lattice relaxation was extremely slow in bulk MgH_2 (Figure 6e), and three orders of magnitude faster in the nanocomposites (Figure 6f). However, the faster relaxation in the nanocomposites cannot be exclusively attributed to hydrogen mobility alone, since it was a combined result of hydrogen mobility, the presence of paramagnetic centers in the carbon support and short ^{1}H spin-diffusion distances in the nanocomposites.

Detailed comparison of the NMR line shape of the nanocomposites with that of bulk MgH_2 (Figure 6a–d) suggests

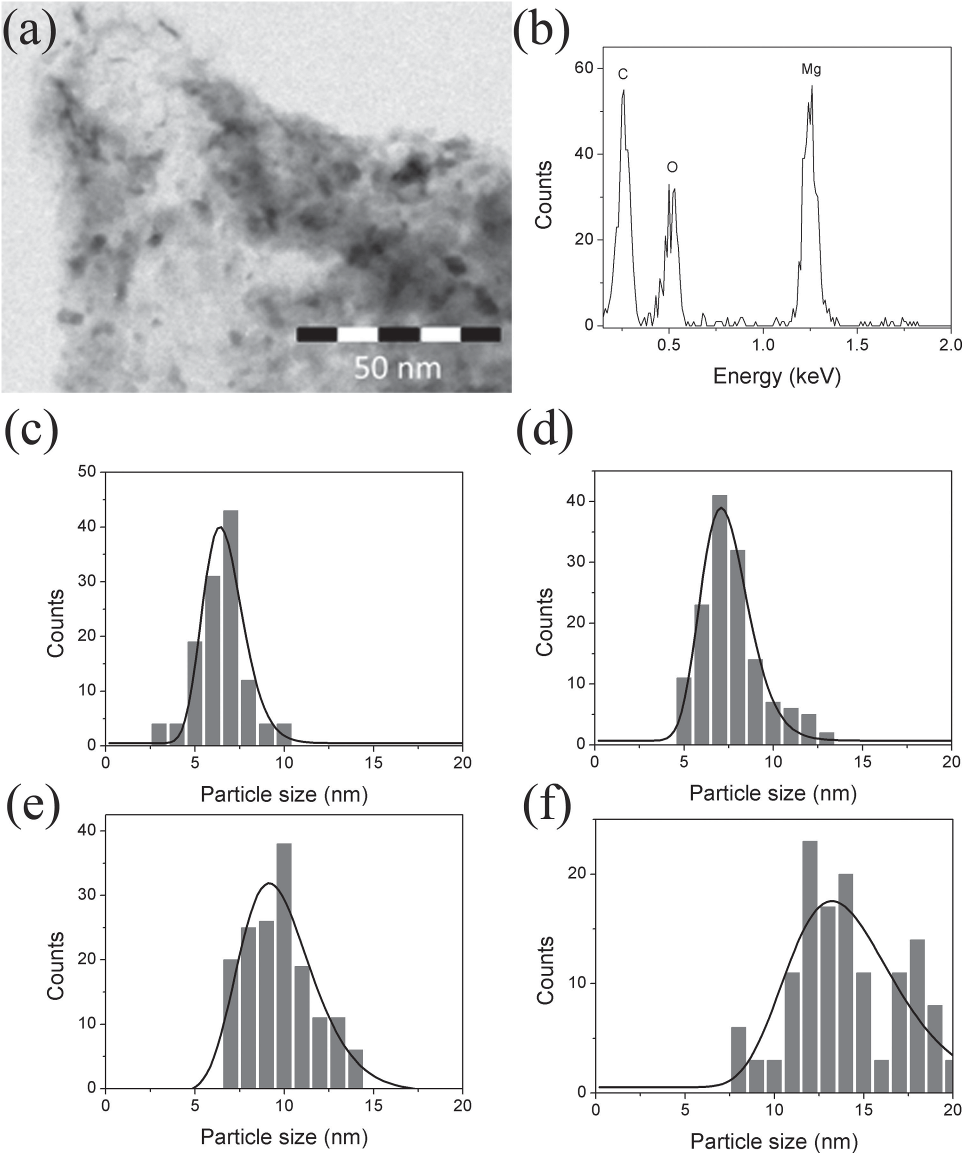

Figure 3. a) Bright field TEM image of MgH_2/CA-6. b) EDX measurement on (a) and nanoparticle size distribution of c) MgH_2/CA-6, d) MgH_2/CA-9, e) MgH_2/CA-12, and f) MgH_2/CA-20. Additional TEM-images are available in Figure S3, Supporting Information. The line represents a log-normal fitting of the particle size distribution.

that the nanocomposite spectra actually reflect a superposition of a relatively narrow and wide (bulk-like) component. This is consistent with the presence of two distinct particle sizes as determined from XRD (Figure S2, Supporting Information) and hydrogen release profiles (Figure 4d). The bimodal character of the nanocomposites in terms of hydrogen mobility was confirmed by the increased line width found in spin-lattice relaxation-weighed spectra (thin black lines in Figure 6a–d). These relaxation-weighed spectra especially reflect the relatively broad resonances from hydrogen atoms with relatively low mobility. Thus, there was a range of hydrogen mobilities, probably caused by varying MgH_2 domain sizes in the nanocomposites. Although the broad line shape features of a bulk-like MgH_2 phase appeared to be recognizable in the static ^1H NMR spectra, the corresponding extremely slow spin-lattice relaxation was not observed for the nanocomposites. Apparently, what looks like "bulk MgH_2" in the ^1H NMR line shape and XRD, still differed from macroscopically bulk MgH_2 in terms of ^1H NMR relaxation, and probably represent the LNPs. Quantitative comparison of the ^1H NMR intensity with an external reference compound (adamantane, 11 wt% hydrogen) allows the total hydrogen capacity of MgH_2/CA-6, MgH_2/CA-9, MgH_2/CA-12, and MgH_2/CA-20 to be roughly estimated as, 65%, 38%, 52%, and 65% respectively. These values were similar to the values determined from TPD (Table S1). Following the same procedure for bulk MgH_2 we obtained a hydrogen content of 6.9 wt%, which is close to the theoretical capacity of 7.6 wt% H_2.

Concluding we see a clear agreement between the solid state NMR results, showing two MgH_2 fractions with clearly

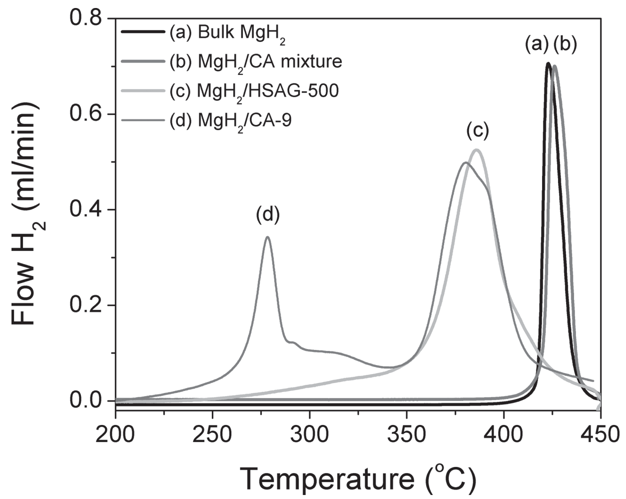

Figure 4. Hydrogen release profiles of a) MgH_2 powder, b) a physical mixture of 10 wt% MgH_2 powder and CA; c) 10 wt% MgH_2 on HSAG and d) 10 wt% MgH_2/CA-9.

different hydrogen mobility (resulting in about three orders of magnitude difference in hydrogen relaxation times) and the structural and hydrogen release data which show two MgH_2 fractions, SNPs and LNPs, which are clearly different in size and hydrogen desorption kinetics. This strongly suggests that the faster hydrogen release for the small MgH_2 nanoparticles can at least partially be attributed to faster hydrogen dynamics in such particles, not only due to decreased solid state diffusion distances, but also due to a higher intrinsic mobility. This is the first time that structural and hydrogen release studies for MgH_2 nanoparticles are combined with intrinsic hydrogen dynamics data.

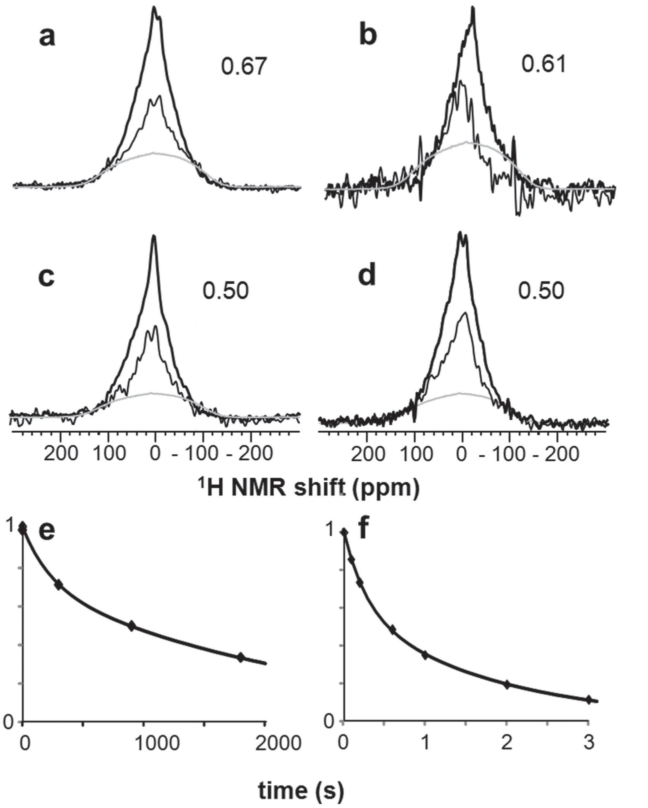

Figure 6. Static ^1H NMR spectra of the 10 wt% MgH_2 on a) CA-6, b) CA-9, c) CA-12, and d) CA-20; e,f) spin-lattice relaxation curves of e) bulk MgH_2 and f) 10 wt% MgH_2/CA-20. In addition to the quantitative ^1H NMR spectra (thick black lines) figure panels a-d also show the corresponding spin-lattice relaxation weighed spectra (thin, noisy black lines) recorded with a z-filter time of 1 s, as well as the broad resonance line shape of bulk MgH_2 (grey line) for comparison.

2.3. Hydrogen Cycling Properties of Nano-Mg(H_2) (<20 nm)

We now discuss specifically the hydrogen cycling properties of the SNPs. The left frame in **Figure 7** shows the hydrogen absorption of Mg(H_2)/CA-9 performed at 300 °C in 18 bar H_2, for 3 subsequent cycles. An absorption measurement on bulk MgH_2 was added as reference. Bulk MgH_2 only had absorbed 0.25 wt% H_2 after 1 h, while Mg(H_2)/CA-9 was able to absorb ≈1.75 wt% of hydrogen within 1 h. This is approximately the amount of hydrogen released by the SNPs in MgH_2/CA-9 at low temperatures (Table S1, Supporting Information).

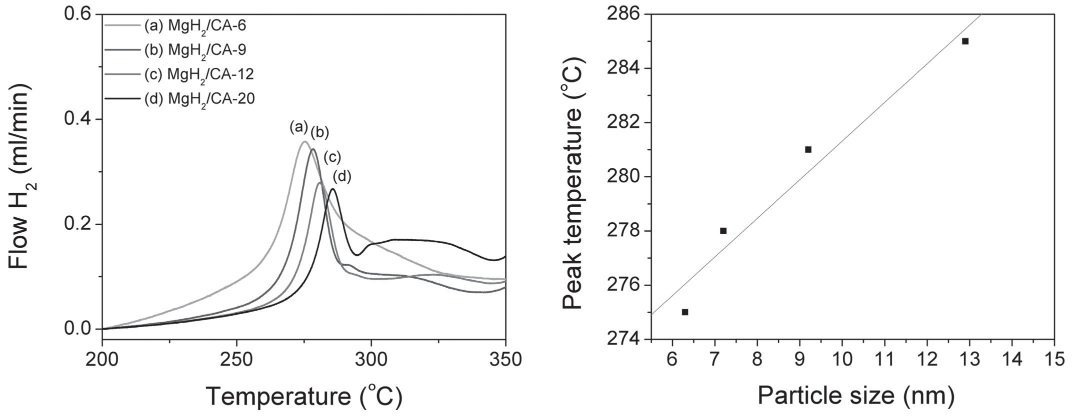

Figure 5. Left: Hydrogen release profiles of 10 wt% MgH_2 on a) CA-6, b) CA-9, c) CA-12, and d) CA-20. Right: Relation between peak temperature and average nanoparticle size for hydrogen desorption.

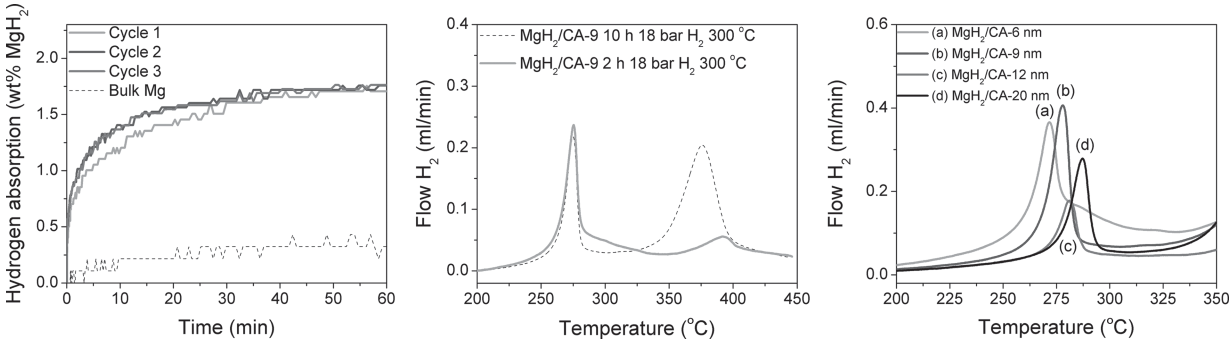

Figure 7. Left: Absorption kinetics of 10 wt% Mg/CA-9 measured volumetrically at 300 °C and 18 bar H_2. Three absorption-desorption cycles were measured subsequently. The absorption of MgH_2 powder (± 37 µm) is shown as reference. Middle: Hydrogen release profiles of 10 wt% MgH_2/CA-9 after different first H_2 absorption durations of 2 h and 10 h. Right: Hydrogen release from 10 wt% nano-MgH_2 on a) CA-6, b) CA-9, c) CA-12, and d) CA-20 after 4 hydrogen sorption cycles at 300 °C. Absorption and desorption was performed at 18 bar and 0.3 bar H_2, respectively. Full desorption profiles are available in Figure S7, Supporting Information.

The effect of different absorption times was compared by measuring the hydrogen release profiles in Figure 7: middle frame. Interestingly, the same peak at low temperature (≈280 °C) was clearly present after hydrogenating for 2 h and almost no hydrogen release was found at higher temperatures. However, after hydrogenating for 10 h the peak at ≈390 °C was present again. A small amount of hydrogen was absorbed by the large Mg particles after 2 h, which is in line with the slow absorption rate of the Mg reference with a powder size in the range micrometers (Figure 7: left). These results clearly show that not only the hydrogen desorption, but also the hydrogen absorption kinetics are strongly affected by the particle size. The large difference in hydrogen sorption rates allows for a selective study on the cycling behavior of the SNPs.

Subsequent absorption cycles were performed on MgH_2/CA-9 (Figure 7: left). Within 15 min, the first cycle absorbed ≈1.3 wt%, while the other cycles have reached a higher capacity after the same time (≈1.5 wt%). Possibly, the Mg phase became more accessible for hydrogen molecules to enter the crystal lattice after the first cycle. This result is comparable to MgH_2/CA nanocomposites prepared by solution impregnation[31] and shows that these Mg(H_2) nanoparticles have an excellent cycling stability with its improved kinetics maintained.

After performing 4 absorption and desorption cycles, hydrogen release for all MgH_2/CA composites was measured again to compare between the performance of the first cycle and after 4 cycles. The right frame in Figure 7 shows the desorption profiles and interestingly, the peaks at low temperatures were still present with similar peak temperatures. Almost no capacity loss was observed, which indicate that no side reactions took place; and no loss in kinetic performance occurred. Thus, the Mg(H_2) nanoparticles showed excellent cycling stability over 4 cycles.

3. Conclusion

Carbon aerogels with different pore size distributions were synthesized and MgH_2 nanoparticles were deposited by heating a mixture of MgH_2 with the carbon aerogels. A bimodal distribution of MgH_2 particles was obtained on the different CAs, which could be distinguished as small nano-MgH_2particles (<20 nm) and larger particles. The small nanoparticles had a size between 3 to 20 nm and the size was correlated to the pore size of the carbon support. Hydrogen sorption measurements showed a large difference in the hydrogen sorption rates for the two different particle size regimes. The peak temperature for hydrogen desorption of the Mg/CA composites varied around 280 °C depending on the pore size of the CA, while temperatures near 400 °C were observed for the larger nanoparticles. Within the small nanoparticle population, the larger the particle, the higher the hydrogen desorption temperatures. Also, the^{1}H wideline NMR spectra clearly showed that the hydrogen dynamics depended on the particle size of MgH_2 with 3 orders of magnitude faster hydrogen dynamics for the small nanoparticles.

Hydrogen storage in the small MgH_2nanoparticles was completely reversible for at least 4 cycles. A capacity of ≈80% was absorbed within 15 min for the Mg nanoparticles at 300 °C with 18 bar H_2This study shows for the first time a clear relation between MgH_2 particle size and hydrogen desorption rates, combined with hydrogen mobility data for the different MgH_2 sizes.

4. Experimental Section

Preparation of the Carbon Aerogels: The carbon aerogels (CAs) were synthesized through resorcinol-formaldehyde condensation catalyzed by sodium carbonate, as reported by Pekala et al. [33] Resorcinol (Sigma Aldrich 99%, 8.65 g, 79 mmol), formaldehyde (Fisher chemical, analytical reagent 37–41%, stabilized by 12% methanol, 12.89 g, 158 mmol) and sodium carbonate (Across organics 99.5%, 0.017 g, 0.16 mmol) were dissolved in deionized water. In order to obtain CAs with different pore size distributions, the amount of water was varied from 40, 45, 50, to 55 wt% with respect to the total weight including the weight of the resorcinol-formaldehyde mixture. After aging (1 day at room temperature, 1 day at 60 °C and 3 days at 90 °C) the samples were cooled, powdered and immersed in acetone to replace the water inside the pores of the formed polymer (3 times, soak time: 1 h, 1 h, 8 h) as described by Li et al.[34] The samples were dried at room temperature and then pyrolyzed in a tubular oven at 800 °C for 10 h in an Ar-flow. All CA samples were stored in an Ar-glovebox (MBraunLabmaster) and all further preparation steps and measurements were performed in inert atmosphere.

Preparation of MgH2/CA Nanocomposites: In a typical experiment, 900 mg of CA was mixed and ground with 100 mg of MgH_2 (Alfa Aesar (98%)) in a mortar, to obtain a 10 wt% MgH_2/CA mixture. The mixture was placed in a graphite cup, which was placed inside a closed stainless steel sample holder, and was heated in a tubular oven with 10 °C min^{-1} to 658 °C and kept at the maximum temperature for 24 min under an Ar flow. Hydrogenation of the samples was performed at 80 bar H_2, 300 °C for 10 h in an autoclave (Parr). The hydrogenated samples were used for structural characterization, NMR and dehydrogenation experiments.

Characterization: Porosity measurements on the carbon aerogels and MgH_2/CA nanocomposites were performed by N_2-physisorption. The samples were loaded in airtight-quartz tubes inside the glove box and measured at −196 °C, using a Micromeritics Tristar 3000 apparatus. The pore size distributions of the samples were obtained by performing Barrett-Joyner-Halenda (BJH) analysis using a Carbon Black thickness-equation as reference on the adsorption branch. The total pore volume was obtained at $p/p_0 = 0.997$. For removal of Mg species, the sample was stirred in an aqueous HCl solution (pH ≈ 2.5) overnight at room temperature, followed by filtering and drying in Ar at 200 °C overnight before this sample was measured.

X-ray diffraction (XRD) patterns were obtained at room temperature from 25° to 105° 2θ (Bruker D8 Advance equipped with VANTEC-1 detector using $Co_K\alpha_{1,2}$ radiation) with a step size of 0.1° per step and an acquisition time of 2 s per step. The samples were measured in an airtight sample holder. For quantitative analysis, Si-powder (Sigma Aldrich, 99.9%) was added as internal standard and Rietveld refinement was performed with the Rietica program.[35]

Differential scanning calorimetry (DSC) measurements were carried out on a physical mixture of MgH_2 and CA (Mettler Toledo HP-DSC 1). Graphite sample holders (TA instruments, 40 μL) were used and loaded with approximately 10 mg of sample. The sample was heated from room temperature to 680 °C followed by a cooling step to room temperature with 5 °C min^{-1} in an Ar-flow of 20 mL min^{-1}.

Transmission electron microscopy (TEM) analysis was performed using an FEI Tecnai 20F FEG microscope operated at 200 kV. Images were obtained in bright field mode with energy-dispersive X-ray spectroscopy (EDX) performed during the same measurement. The samples were prepared by grinding in a mortar extensively, before the dry powders were applied on a 200 mesh copper grid with a carbon coated polymer film in the glove box. The samples were exposed to air for no more than 5 s during insertion of the probe into the electron microscope. Histograms for the average size of the nanoparticles were obtained by measuring manually ≈150 particles below 20 nm.

Hydrogen Sorption Measurements: The hydrogen desorption properties of the MgH_2/CA composites were studied with temperature programmed desorption (TPD) using a Micromeritics AutoChem II 2920 apparatus equipped with a TCD detector. Approximately 100 mg of the sample was used for each measurement. The samples were heated up to 450 °C with 5 °C min^{-1} in 25 mL min^{-1} Ar- flow.

The hydrogen absorption kinetics were measured directly on the as prepared Mg/CA samples using a Sievert apparatus (Setaram PCT PRO-2000). A steel holder was used (≈4.8 mL), where the inner walls were covered with graphite foil (PAPYEX) to avoid side reactions. The hydrogen absorption conditions were 300 °C at ≈18 bar H_2 pressure for 3 h. Before starting the next absorption cycle, the sample was kept at 300 °C in vacuum for several hours to allow full hydrogen desorption from the samples.

NMR Spectroscopy: Wideline ^1H NMR spectra were recorded at room temperature without sample rotation on a Bruker DRX200 spectrometer operating at a ^1H NMR frequency of 200 MHz, and equipped with a probe head with a 5 mm horizontal coil. To obtain undistorted line shapes we employed a magic-sandwich-echo pulse sequence preceded by two 90° pulses with alternatingly same and opposite phases [36]:

$$90^\circ_{+x}90^\circ_{\pm x} - T - 90^\circ_{\phi} - \tau - 90^\circ_{\psi} - \left(\tau_{MSE} - 90^\circ_{\phi} - \tau_{MSE}\right)_4$$

$$\left(\tau_{MSE} - 90^\circ_{-\phi} - \tau_{MSE}\right)_4 - 90^\circ_{\psi} - \tau - \text{detection}_{\pm\phi}$$

where the pulse phases ϕ and ψ are related by 90° phase shift, $\psi = \phi + 90^\circ$. The 90° pulse duration was 2 μs, and the pulse intervals τ and τ_{MSE}, were 8 and 2 μs, respectively, whereby τ also includes the pre-detection delay of 5.5 μs. Combined with a proper phase cycle of ϕ and ψ, the initial $90^\circ_{+x} - 90^\circ_{\pm x}$ pulse pair effectively prevents the accumulation of the tail of the last pulse into the first points of the echo and ensures a flat baseline in this way. For quantitative purpose the (z-filter) time T following the initial two pulses was taken 10 ms, which is large compared to proton transversal relaxation T_2, but negligibly short with respect to the spin-lattice relaxation T_1. T_1 – weighed spectra were recorded with T = 1 s, and T_1 relaxation was measured by varying T. The relaxation delay between subsequent NMR scans was taken 3600 s for bulk MgH_2 and 900 s for the nanocomposites.

Supporting Information

Supporting Information is available from the Wiley Online Library or from the author.

Acknowledgements

This work was financially supported by a grant from the Dutch organization for scientific research (NWO VIDI 016.072.316). The authors would like to acknowledge M. van Zwienen and J. D. Meeldijk for their technical support in the hydrogen sorption measurement; and for obtaining the TEM images.

Received: December 3, 2013
Revised: January 14, 2014

---

[1] International Energy Agency, Monthly Electricity Statistics, http://www.iea.org/newsroomandevents/newsletters/ (accessed: 03, 2013).
[2] G. W. Crabtree, M. S. Dresselhaus, M. V. Buchanan, *Phys. Today* **2004**, *57*, 39–44.
[3] P. Larsson, C. M. Araújo, J. A. Larsson, P. Jena, R. Ahuja, *Proc. Natl. Acad. Sci. U.S.A.* **2008**, *105*, 8227–8231.
[4] G. Mao, X. Hu, X. Wu, Y. Dai, S. Chu, J. Deng, *Int. J. Hydrogen Energy* **2011**, *36*, 8388–8391.
[5] M. Felderhoff, B. Bogdanovic, *Int. J. Mol. Sci.* **2009**, *10*, 335–344.
[6] McPhy Energy, Solid-hydrogen-storage, http://www.mcphy.com/en/technologies/solid/hydrogen/storage/ (accessed: 11, 2012).
[7] Q. A. Zhang, H. Y. Wu, *Mater. Chem. Phys.* **2005**, *94*, 69–72.
[8] U. Haussermann, H. Blomqvist, D. Noréus, *Inorg. Chem.* **2002**, *41*, 3684–3692.
[9] Z. Wu, M. D. Allendorf, J. C. Grossman, *J. Am. Chem. Soc.* **2009**, *131*, 13918–13919.
[10] P. Vajeeston, P. Ravindran, M. Fichtner, H. Fjellvåg, *J. Phys. Chem. C* **2012**, *116*, 18965–18972.
[11] R. W. P. Wagemans, J. H. Van Lenthe, P. E. De Jongh, A. J. Van Dillen, K. P. De Jong, *J. Am. Chem. Soc.* **2005**, *127*, 16675–16680.
[12] M. Paskevicius, D. A. Sheppard, C. E. Buckley, *J. Am. Chem. Soc.* **2010**, *132*, 5077–5083.
[13] V. Bérubé, G. Radtke, M. Dresselhaus, G. Chen, *Int. J. Energy Res.* **2007**, *31*, 637–663.
[14] L. E. A. Berlouis, P. Honnor, P. J. Hall, S. Morris, S. B. Dodd, *J. Mater. Sci.* **2006**, *41*, 6403–6408.
[15] D. Chen, L. Chen, Y. Wang, S. Liu, D. Chen, C. Ma, L. Wang, *Xiyou Jinshu Cailiao Yu Gongcheng/Rare Metal Materials and Engineering* **2004**, *33*, 485–489.

[16] O. Gutfleisch, S. Dal Toè, M. Herrich, A. Handstein, A. Pratt, *J. Alloys Compd.* **2005**, *404–406*, 413–416.

[17] N. Hanada, T. Ichikawa, H. Fujii, *J. Alloys Compd.* **2005**, *404–406*, 716–719.

[18] T. R. Jensen, A. Andreasen, T. Vegge, J. W. Andreasen, K. Ståhl, A. S. Pedersen, M. M. Nielsen, A. M. Molenbroek, Flemming Besenbacher, *Int. J. Hydrogen Energy* **2006**, *31*, 2052–2062.

[19] W. Oelerich, T. Klassen, R. Bormann, *J. Alloys Compd.* **2001**, *315*, 237–242.

[20] P. H. L. Notten, M. Ouwerkerk, H. Van Hal, D. Beelen, W. Keur, J. Zhou, H. Feil, *J. Power Sources* **2004**, *129*, 45–54.

[21] S. D. Beattie, U. Setthanan, G. S. McGrady, *Int. J. Hydrogen Energy* **2011**, *36*, 6014–6021.

[22] P. Ngene, R. Van Zwienen, P. E. De Jongh, *Chem. Commun.* **2010**, *46*, 8201–8203.

[23] P. Adelhelm, J. Gao, M. H. W. Verkuijlen, C. Rongeat, M. Herrich, P. J. M. Van Bentum, O. Gutfleisch, A. P. M. Kentgens, K. P. De Jong, P. E. De Jongh, *Chem. Mater.* **2010**, *22*, 2233–2238.

[24] J. Gao, P. Adelhelm, M. H. W. Verkuijlen, C. Rongeat, M. Herrich, P. J. M. Van Bentum, O. Gutfleisch, A. P. M. Kentgens, K. P. De Jong, P. E. De Jongh, *J. Phys. Chem. C* **2010**, *114*, 4675–4682.

[25] P. E. De Jongh, P. Adelhelm, *ChemSusChem* **2010**, *3*, 1332–1348.

[26] P. E. De Jongh, R. W. P. Wagemans, T. M. Eggenhuisen, B. S. Dauvillier, P. B. Radstake, J. D. Meeldijk, J. W. Geus, K. P. De Jong, *Chem. Mater.* **2007**, *19*, 6052–6057.

[27] C. Zlotea, C. Chevalier-César, E. Léonel, E. Leroy, F. Cuevas, P. Dibandjo, C. Vix-Guterl, T. Martens, M. Latroche, *Faraday Discuss.* **2011**, *151*, 117–131.

[28] M. Konarova, A. Tanksale, J. Norberto Beltramini, G. Qing Lu, *Nano Energy* **2013**, *2*, 98–104.

[29] T. K. Nielsen, K. Manickam, M. Hirscher, F. Besenbacher, T. R. Jensen, *ACS Nano* **2009**, *3*, 3521–3528.

[30] M. Paskevicius, H. Tian, D. A. Sheppard, C. J. Webb, M. P. Pitt, E. M. Gray, N. M. Kirby, C. E. Buckley, *J. Phys. Chem. C* **2011**, *115*, 1757–1766.

[31] Y. Liu, J. Zou, X. Zeng, X. Wu, H. Tian, W. Ding, J. Wang, A. Walter, *Int. J. Hydrogen Energy* **2013**, *38*, 5302–5308.

[32] S. Srinivasan, P. C. M. M. Magusin, R. A. Van Santen, P. H. L. Notten, H. Schreuders, B. Dam, *J. Phys. Chem. C* **2011**, *115*, 288–297.

[33] R. W. Pekala, *J. Mater. Sci.* **1989**, *24*, 3221–3227.

[34] W. C. Li, A. H. Lu, C. Weidenthaler, F. Schüth, *Chem. Mater.* **2004**, *16*, 5676–5681.

[35] B. A. Hunter, *IUCR Powder Diffraction* **1997**, *22*, 21.

[36] M. H. W. Verkuijlen, P. Ngene, D. W. De Kort, C. Barré, A. Nale, E. R. H. Van Eck, P. J. M. Van Bentum, P. E. De Jongh, A. P. M. Kentgens, *J. Phys. Chem. C* **2012**, *116*, 22169–22178.